Phosphatases control PKA-dependent functional microdomains at the outer mitochondrial membrane

Alex Burdyga[a], Nicoletta C. Surdo[b,1], Stefania Monterisi[b,1], Giulietta Di Benedetto[c,d], Francesca Grisan[c,d], Elisa Penna[e], Luca Pellegrini[e], Mario Bortolozzi[d,f], Pawel Swietach[b,g], Tullio Pozzan[c,d,h,2], and Konstantinos Lefkimmiatis[c,d,g,2]

[a]West Midlands Regional Genetics Laboratory, Birmingham Women's and Children's Hospital, B15 2TG Birmingham, United Kingdom; [b]Department of Physiology, Anatomy and Genetics, Burdon Sanderson Cardiac Science Centre, OX1 3PT Oxford; [c]Padua Section, Neuroscience Institute, National Research Council, 35121 Padua, Italy; [d]Foundation for Advanced Biomedical Research, Venetian Institute of Molecular Medicine, 35129 Padua, Italy; [e]Department of Molecular Biology, Medical Biochemistry and Pathology, Faculty of Medicine, Universitè Laval, Quebec, QC G1V 0A6, Canada; [f]Department of Physics and Astronomy, University of Padua, 35122 Padua, Italy; [g]Department of Physiology, Anatomy and Genetics, British Heart Foundation Centre of Research Excellence, OX1 3PT Oxford, United Kingdom; and [h]Department of Biomedical Sciences, University of Padua, 35121 Padua, Italy

Contributed by Tullio Pozzan, May 30, 2018 (sent for review April 13, 2018; reviewed by Shmuel Muallem and David I. Yule)

Evidence supporting the heterogeneity in cAMP and PKA signaling is rapidly accumulating and has been largely attributed to the localization or activity of adenylate cyclases, phosphodiesterases, and A-kinase–anchoring proteins in different cellular subcompartments. However, little attention has been paid to the possibility that, despite homogeneous cAMP levels, a major heterogeneity in cAMP/PKA signaling could be generated by the spatial distribution of the final terminators of this cascade, i.e., the phosphatases. Using FRET-based sensors to monitor cAMP and PKA-dependent phosphorylation in the cytosol and outer mitochondrial membrane (OMM) of primary rat cardiomyocytes, we demonstrate that comparable cAMP increases in these two compartments evoke higher levels of PKA-dependent phosphorylation in the OMM. This difference is most evident for small, physiological increases of cAMP levels and with both OMM-located probes and endogenous OMM proteins. We demonstrate that this disparity depends on differences in the rates of phosphatase-dependent dephosphorylation of PKA targets in the two compartments. Furthermore, we show that the activity of soluble phosphatases attenuates PKA-driven activation of the cAMP response element-binding protein while concurrently enhancing PKA-dependent mitochondrial elongation. We conclude that phosphatases can sculpt functionally distinct cAMP/PKA domains even in the absence of gradients or microdomains of this messenger. We present a model that accounts for these unexpected results in which the degree of PKA-dependent phosphorylation is dictated by both the subcellular distribution of the phosphatases and the different accessibility of membrane-bound and soluble phosphorylated substrates to the cytosolic enzymes.

phosphatases | mitochondria | PKA | cAMP | signaling

To achieve specificity of function, elements of the cAMP signaling cascade are strategically organized into distinct signaling units called "microdomains" (1). The subcellular organization and range of cAMP signals is strongly influenced by A-kinase–anchoring proteins (AKAPs) (2), a family of proteins that tether PKA and regulatory elements of the cAMP cascade to specific cellular sites (3). While AKAPs provide the physical framework for allowing highly localized PKA activity, the availability of cAMP in these microdomains is controlled primarily by phosphodiesterase (PDE) activity (4). Thus, in response to cAMP-elevating stimuli, PDE activity/localization can determine the level of cAMP attained within a microdomain and eventually can degrade the messenger once the underlying stimulus has subsided (5). Crucially, cAMP degradation and PKA inactivation do not per se terminate the cascade; this ultimately depends on the dephosphorylation of PKA targets by phosphatases (6–8).

In its inactive form, PKA is a heterotetramer of two catalytic (PKA-C) and two regulatory (PKA-R) subunits. Four types of regulatory subunits have been described, RIα, RIβ, RIIα, and RIIβ (9). PKA-Rs confer a number of important properties to the PKA holoenzyme. For instance, PKA tetramers containing the RI types are activated at lower [cAMP] compared with those including the RII types (10). The more cAMP-sensitive RI-based holoenzymes are found predominantly in the soluble fraction of the cell, whereas RII-based enzymes, with higher activation thresholds, are found in the particulate fractions (11). Previous studies have shown that cAMP produced at the plasma membrane by adenylyl cyclases (ACs) (12) is able to activate high-threshold AKAP-bound PKAs [e.g., at the outer mitochondrial membrane (OMM)] without eliciting low-threshold cytosolic PKA activity en route, but the mechanism underlying this apparent shielding effect is still not well understood (13). Here, we use live-cell imaging and biochemistry to interrogate the mechanisms that selectively control the phosphorylation level and duration of PKA targets.

Results

cAMP Induces Higher PKA-Dependent Phosphorylation at the OMM than in the Cytosol in HeLa Cells. To compare the activation of OMM-tethered and soluble (cytosolic) PKAs, we used FRET-based sensors to monitor changes in cAMP and PKA-dependent

Significance

The selective phosphorylation of spatially distinct PKA targets is key for the pleiotropy of the cAMP cascade. This characteristic of the pathway is currently attributed to the ability of phosphodiesterases or adenylate cyclases to create subcellular sites (microdomains) where the concentration of cAMP is distinct from that of the surrounding areas. The role of phosphatases in this process has not been tested. Here we show that limited access of phosphatases to the PKA targets present at the outer mitochondrial membrane generates distinct microdomains of PKA phosphorylated proteins despite there being no differences in the local cAMP levels. These results describe an alternative mechanism capable of generating functional cAMP/PKA-dependent microdomains and may be extrapolated to the compartmentalization of other kinase-dependent events.

Author contributions: A.B., G.D.B., T.P., and K.L. designed research; A.B., N.C.S., G.D.B., F.G., E.P., and K.L. performed research; L.P. and M.B. contributed new reagents/analytic tools; A.B., N.C.S., S.M., G.D.B., F.G., P.S., and K.L. analyzed data; and P.S., T.P., and K.L. wrote the paper.

Reviewers: S.M., National Institutes of Health; and D.I.Y., University of Rochester.

The authors declare no conflict of interest.

This open access article is distributed under Creative Commons Attribution-NonCommercial-NoDerivatives License 4.0 (CC BY-NC-ND).

[1] N.C.S. and S.M. contributed equally to this work.

[2] To whom correspondence may be addressed. Email: tullio.pozzan@pozzanlab.org or konstantinos.lefkimmiatis@cnr.it.

This article contains supporting information online at www.pnas.org/lookup/suppl/doi:10.1073/pnas.1806318115/-/DCSupplemental.

Published online June 25, 2018.

phosphorylation levels in the cytosol and at the OMM. cAMP was monitored by a cAMP sensor, EPAC-S^{H187} (H187) (14–18), and its OMM-targeted variant OMM-H187, whereas PKA-dependent phosphorylation levels were assayed using soluble and OMM-targeted versions of the FRET-based sensor AKAR4 (19).

First, we performed in vitro calibrations to confirm that each pair of sensors produces comparable responses to matching cAMP or PKA phosphorylation levels. Supernatants obtained from lysates of HEK293 cells expressing soluble sensors were uniformly fluorescent, whereas those expressing OMM-targeted sensors displayed particulate fluorescence in well-defined structures (Fig. 1 *A* and *B*, *Insets*). Calibration curves were generated by acquiring the FRET ratio of each sensor before and after incubation with increasing doses of either cAMP (for H187-based sensors) or purified PKA-Cα (for AKAR4-based sensors). As shown in Fig. 1*A*, H187 and OMM-H187 had overlapping calibration curves with the same cooperativity ($n = 1.05 \pm 0.007$ for H187; 1.063 ± 0.06 for OMM-H187) and apparent cAMP-binding constant ($K_{cAMP} = 7.83 \pm 1.45$ μM for H187; 7.40 ± 1.62 μM for OMM-H817), indicating that the process of targeting to the OMM does not alter the sensor's cAMP interaction. Minimal FRET ratios ($R_{min} = 0.25 \pm 0.035$ for H187; 0.24 ± 0.005 for OMM-H187) and maximal FRET ratios ($R_{max} = 0.71 \pm 0.009$ for H187; 0.64 ± 0.038 for OMM-H187) were similarly unaffected by OMM targeting. In the case of AKAR4-based sensors, minimal and maximal ratios were higher in OMM-targeted versions ($R_{min} = 1.72 \pm 0.036$ for AKAR4 and 2.75 ± 0.05 for OMM-AKAR4; $R_{max} = 2.53 \pm 0.06$ for AKAR4 and 3.37 ± 0.043 for OMM-AKAR4), but the levels of PKA-Cα that produced half-maximal sensor activation (K_{PKA}) and the cooperativity of this process were unaffected by OMM targeting ($K_{PKA} = 1{,}221 \pm 138$ units for AKAR4 and $1{,}200 \pm 267$ units for OMM-AKAR4; $n = 2.98 \pm 0.22$ for AKAR4 and 3.002 ± 0.36 for OMM-AKAR4) (Fig. 1*B*).

To compare cAMP responses in cytosolic and OMM domains captured in a single experimental protocol, H187- and OMM-H187–expressing populations of HeLa cells were mixed and plated onto glass coverslips (20). Increasing doses of the broad-spectrum AC activator forskolin (Fsk) produced matching increases in cAMP in both the cytosol and OMM (Fig. 1*C*). Using mixed populations of cells expressing AKAR4 or OMM-AKAR4, we observed that the increases in PKA-dependent phosphorylation were significantly higher at the OMM than in the cytosol (Fig. 1*D*) despite being matched for cAMP levels.

PKA-Dependent Phosphorylation at the OMM of Neonatal Rat Ventricular Myocytes Is Distinct from That in the Cytosol. The existence of domains manifesting distinct patterns of PKA-dependent phosphorylation but without a measurable difference in cAMP levels was tested in neonatal rat ventricular myocytes (NRVMs), a physiologically relevant cellular model for cAMP signaling (5). To adapt the coculture protocol for use with NRVMs, we developed adenoviral versions of the four FRET sensors. As shown in *SI Appendix*, Fig. S1, 18–24 h after plating it was possible to identify cells expressing cytosolic- and OMM-targeted sensors [H187-based (*SI Appendix*, Fig. S1*A*) or AKAR4-based (*SI Appendix*, Fig. S1*B*)] in one field of view. Under basal conditions in NRVMs, the cytosolic- and OMM-targeted sensors reported ratios that were similar to the value of R_{min} determined for these constructs in vitro (Fig. 1 *A* and *B*). Furthermore, saturation of these sensors with Fsk plus the broad-spectrum PDE inhibitor 3-isobutyl-1-methylxanthine (IBMX) evoked responses in NRVMs that were not smaller than R_{max} determined in vitro (*SI Appendix*, Fig. S2). It therefore appears valid to normalize FRET responses to the maximal (saturating) ratio obtained with Fsk/IBMX to compare results from different experiments.

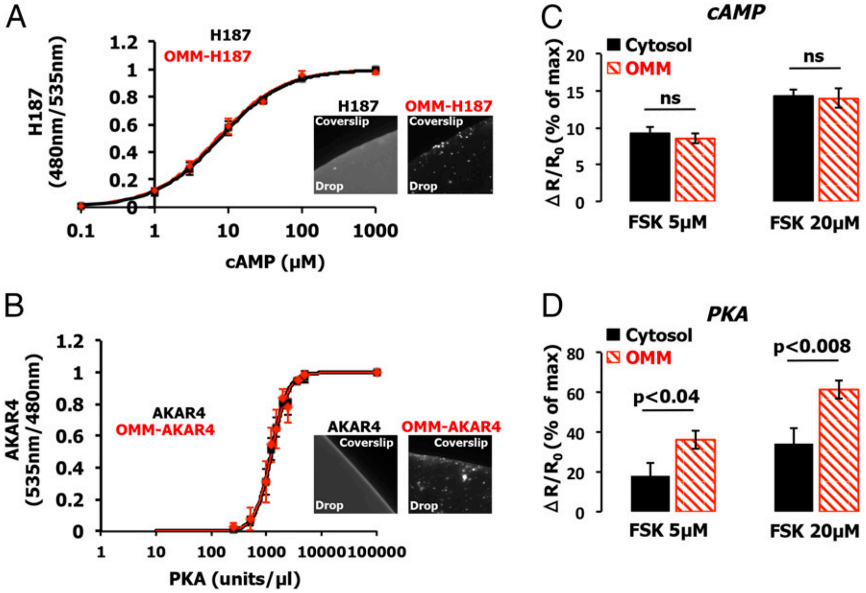

Fig. 1. Small cAMP increases induce higher AKAR4 signals at the OMM of HeLa cells. (*A*) Calibration and comparison of H187 and OMM-H187 sensors. Intracellular buffer containing H187 or OMM-H187 (*Insets*) was complemented with increasing concentrations of cAMP, and FRET ratios were acquired after 10 min incubation. Each data point is the average of four independent experiments. (*B*) Calibration and comparison of AKAR4 and OMM-AKAR4 sensors. Intracellular buffer containing AKAR4 or OMM-AKAR4 (*Insets*) was complemented with increasing doses (units) of PKA catalytic subunit. FRET values were measured after 10–15 min incubation. Each data point is the average of five independent experiments. (*C*) Increases in cAMP produced in response to Fsk were not different at the cytosol or OMM of HeLa cells expressing the cAMP sensors H187 or OMM-H187. Data shown are the average ± SEM of 17 H187-expressing cells or 28 OMM-H187-expressing cells in four independent experiments. ns, not significant. (*D*) PKA-dependent phosphorylation in response to Fsk was higher at the OMM than at the cytosol in mixed populations of HeLa cells. Data are shown as the average ± SEM of 11 AKAR4-expressing cells or 13 OMM-AKAR4–expressing cells in four independent experiments.

As shown in Fig. 2*A*, gradually increasing doses of Fsk induced comparable cAMP responses in the cytosol and OMM of NRVMs. In contrast, when mixed populations of cells expressing AKAR4 or OMM-AKAR4 were challenged with the same Fsk dose–response protocol, the response was significantly greater at the OMM than in the cytosol (Fig. 2*B*), suggesting a functionally distinct pattern of PKA activation to the same underlying cAMP trigger. These findings clearly suggest an additional level contributing to PKA activity compartmentalization, beyond that of cAMP concentration.

Among the factors that may influence the patterns of cAMP signals are the distribution of G protein-coupled receptors (GPCRs) and ACs (21, 22). Fsk, being a direct and nonspecific activator of transmembrane ACs, bypasses the GPCR/AC axis. To engage the canonical GPCR/AC route, we performed experiments with

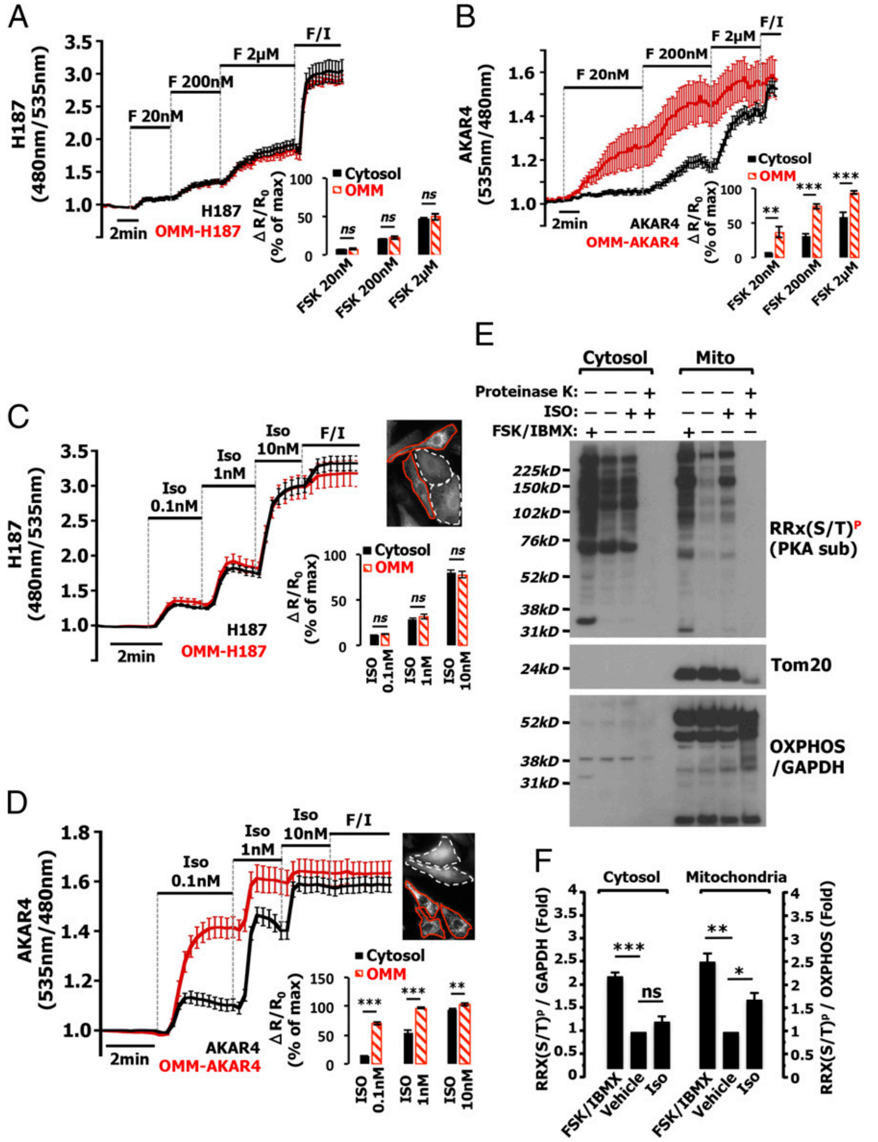

Fig. 2. Iso induces distinct PKA-dependent patterns in the cytosol and OMM without measurable differences in cAMP levels. (*A*) Coculture of cells expressing H187 or OMM-H187 subjected to increasing doses of Fsk. cAMP increases in response to Fsk were not different in the two compartments. (*Inset*) Average ± SEM of 21 H187-expressing cells and 12 OMM-H187-expressing cells in three independent experiments. F/I, Fsk 20 μM combined to IBMX 100 μM; ns, not significant. (*B*) Coculture of cells expressing AKAR4 or OMM-AKAR4 subjected to increasing doses of Iso. AKAR4 signals in response to Iso were significantly higher at the OMM than in the cytosol. (*Inset*) Average ± SEM of 23 AKAR4-expressing cells and eight OMM-AKAR4–expressing cells in three independent experiments. ***$P < 0.001$; ** $P < 0.006$. (*C*) NRVMs expressing H187 or OMM-H187 were challenged with increasing doses of Iso. cAMP increases in response to Iso were not different in the two compartments. (*Upper Inset*) Photomicrograph of a representative field (Magnification: 40×.) (representative ROIs: dotted lines, OMM-H187; solid lines, H187). (*Lower Inset*) Average ± SEM of 28 H187-expressing cells and 18 OMM-H187–expressing cells in three independent experiments. (*D*) NRVMs expressing AKAR4 or OMM-AKAR4 were subjected to increasing doses of Iso. AKAR4 signals in response to Iso were significantly higher at the OMM than in the cytosol. (*Upper Inset*) Photomicrograph of a representative field (Magnification: 40×.) (representative ROIs: dotted lines, OMM-AKAR4; solid lines. AKAR4). (*Lower Inset*) Average ± SEM of 26 AKAR4-expressing cells and 18 OMM-AKAR4–expressing cells in three independent experiments. ***$P < 0.001$; ** $P < 0.005$. (*E*) Cytosolic and mitochondrial fractions of NRVMs treated with Iso or Fsk combined with IBMX or vehicle control (DMSO). The phosphorylation status was assessed by a phospho-PKA substrate antibody, $\text{RRX(S/T)}^{\text{P}}$. The levels of the OMM marker Tom20 indicated efficient Proteinase K digestion. Purity and loading of the mitochondrial fractions were tested using an antibody mixture against the rodent OXPHOS subunits; GAPDH was used as a cytosolic marker. (*F*) Intensities of phospho-bands normalized to GAPDH for the cytosol or to OXPHOS for the mitochondria (five independent NRVM cultures). ***$P < 0.001$; ** $P < 0.002$; *$P < 0.02$).

β-adrenoreceptor agonists. Mixed NRVMs expressing H187 or OMM-H187 (photomicrograph in Fig. 2*C*) were challenged with increasing doses of isoproterenol (Iso), a β1- and β2-adrenoreceptor agonist. As with Fsk, Iso produced comparable cAMP levels at the OMM and in the cytosol (Fig. 2*C* and Movie S1). In agreement with the data obtained with Fsk, for matching levels of cAMP, higher PKA-dependent phosphorylation was reported for OMM-AKAR4 than for its cytosolic variant (Fig. 2*D* and Movie S2). These results indicate that the greater response registered with OMM-AKAR4 is not related to differences in the means by which the ACs are activated. Moreover, the similarity in cAMP responses to Iso and Fsk argues against differential handling of the second messenger in cytosolic and OMM compartments by PDEs. In line with this model, increasing doses of IBMX induced similar responses of OMM-H187 and H187 (*SI Appendix*, Fig. S3*A*) but higher AKAR4 signals at the OMM than in the cytosol (*SI Appendix*, Fig. S3*B*). Since broad-spectrum inhibition of PDE activity produces a nearly uniform increase in cAMP, compartmentalization of the messenger cannot explain the differences in PKA-dependent phosphorylation of AKAR4 recorded at the OMM and in the cytosol.

AKAR4 sensors are based on an optimized PKA consensus (23) which may not be representative of the entire array of native PKA phosphorylation sites (24). To test whether the compartment-specific PKA actions reported by OMM-AKAR4 recapitulate the phosphorylation of endogenous PKA targets, NRVMs were treated with vehicle (negative control), low doses of Iso (100 pM), or 20 μM Fsk and 100 μM IBMX (positive control). After treatment, mitochondrial and soluble protein fractions were isolated, and Western blotting was performed to test for changes in PKA-dependent phosphorylation of the endogenous proteins present in these two fractions. As shown in Fig. 2*E*, low-dose (100 pM) Iso induced a strong phosphorylation pattern in mitochondria compared with the vehicle control, whereas proteins in the soluble fraction were unaffected. We also noted that the cytosolic fraction presented higher background at the steady state that was H89 insensitive and therefore PKA independent (*SI Appendix*, Fig. S3*C*). In contrast, Fsk/IBMX induced strong phosphorylation in both fractions (quantified in Fig. 2*F*). Our OMM-AKAR4 sensor is designed to measure PKA-dependent phosphorylation at the OMM; however PKA has been reported in all mitochondrial compartments, including the intermembrane space (IMS) and, controversially, in the matrix (19, 25–27). To resolve the contribution from each mitochondrial compartment, Iso-treated fractions were exposed to Proteinase K, which cleaves proteins of the OMM only. This treatment abolished the phosphorylation of the endogenous targets and drastically decreased the level of OMM marker Tom20 without affecting the levels of intramitochondrial proteins (oxidative phosphorylation, OXPHOS) (Fig. 2*E*). Similar experiments performed using HeLa cells confirmed the results obtained in NRVMs (*SI Appendix*, Fig. S3*D*). These experiments are in line with measurements obtained using OMM-AKAR4 and suggest that, under our experimental conditions (low doses of GPCR agonist), the majority of mitochondrial cAMP/PKA-dependent phosphorylation detected is from the OMM; a possible small contribution from the IMS cannot be unequivocally excluded, while the contribution of the matrix-borne PKA is undetectable.

Phosphatases Differentially Affect PKA Action in the Cytosol and at the OMM. Having shown that the differences observed in PKA-dependent phosphorylation between the cytosol and OMM do not depend on the levels of the diffusible messenger, controlled by the GPCR/AC/PDE axis, we tested the involvement of other regulatory elements of the cAMP pathway. We performed a qualitative analysis of the cAMP signaling components present in the cytosol and mitochondria of NRVMs by Western blot. Both the cytosol and mitochondria contained the main PKA catalytic type (PKA-Cα) (9) as well as RII regulatory subunits Fig. 3*A*). Paradoxically, the majority of PKA-RI subunits, which are responsive to lower cAMP levels and would predict higher PKA activation at low cAMP elevations (10), were more abundant in the cytosol, despite the lower PKA action detected therein.

Having excluded the elements contributing to cAMP elevations and hence PKA activation, we turned our attention to those elements that can counteract PKA activity, that is, PDEs and phosphatases. To compare the degradation of cAMP at the OMM and cytosol, mixed populations of NRVMs expressing the two versions of H187 were treated with increasing doses of Iso (to increase cAMP levels submaximally) or with Fsk/IBMX that consistently saturate all sensors. Once an equilibrium was reached, the stimulus was washed away to terminate cAMP production and, in the case of Fsk/IBMX, to release the activity of the PDEs (previously blocked by IBMX). As shown in *SI Appendix*, Fig. S4 *A* and *B*, cAMP degradation measured by OMM-H187 matched the kinetics measured by cytosolic H187, indicating that cAMP is degraded at the same rate in both compartments. We repeated the Fsk/IBMX saturating protocol with cells expressing AKAR4 or OMM-AKAR4. After saturating the sensors with Fsk/IBMX, we monitored the phosphatase-dependent signal recovery upon stimulus washout. As shown in Fig. 3*B*, phosphatases promptly dephosphorylated soluble AKAR4, while the signal of AKAR4 at the OMM persisted for a longer time before eventually reaching basal levels. These experiments suggest the possible involvement of phosphatases in the mechanisms through which cAMP elicits different levels of PKA-dependent phosphorylation in OMM and cytosol of NRVMs.

To test for the presence of phosphatases in the cytosolic and mitochondrial fractions, we performed Western blot experiments using specific antibodies for the principal cardiac phosphatases PP2A, PP1, and PP2B (calcineurin) (6, 7) that are responsible for >90% of protein phosphatase activity in cardiac myocytes (7). As shown in Fig. 3*C*, we detected a strong presence of all three proteins in the cytosol, whereas the mitochondrial fractions of NRVMs contained undetectable levels of PP2B and PP2A and negligible PP1 (28).

Next, to test more directly whether phosphatases were responsible for compartmentalized PKA-dependent phosphorylation, we challenged mixed NRVM cells expressing AKAR4 or OMM-AKAR4 with low (20 nM) levels of Fsk alone or in combination with calyculin A (CalA; an inhibitor of PP2A and PP1) and cyclosporine A (CsA; a PP2B inhibitor;). As shown in Fig. 3*D* and Movie S3, 20 nM Fsk induced a significant increase in OMM-AKAR4 phosphorylation, while cytosolic AKAR4 phosphorylation remained at basal levels. Upon the addition of a mix of CalA and CsA, we observed an increase in the FRET signal from both sensors; however, the response at the cytosol was dramatically enhanced upon phosphatase inhibition. Interestingly, the signal induced by 20 nM Fsk in the presence of CalA and CsA was similar with both sensors, demonstrating that upon phosphatase inhibition the two compartments attain comparable levels of PKA-dependent phosphorylation (Fig. 3*D*).

PP2A and PP1 are considered the major regulators of cytosolic PKA in NRVMs (6), while PP2B counteracts the actions of PKA on mitochondrial morphology (29, 30). In addition, it was recently suggested in insulin-secreting MIN6 β cells that, in response to Ca^{2+}/calmodulin, PP2B remains active for longer periods in the cytosol than in the endoplasmic reticulum (ER) and mitochondria. These data, arguing for the existence of two subcellular zones characterized by high (cytosol) and low (ER/mitochondria) PP2B activity (31), may explain our findings in NVRMs. Therefore, we performed a series of experiments aiming to dissect the involvement of PP2B in the compartmentalized PKA actions observed between cytosol and mitochondria. Using the protocol shown in Fig. 3*D*, we combined 20 nM Fsk with CalA to block PP2A and PP1 or, alternatively, 20 nM Fsk with CsA to block PP2B selectively. As shown in *SI Appendix*, Fig. S4*C*,

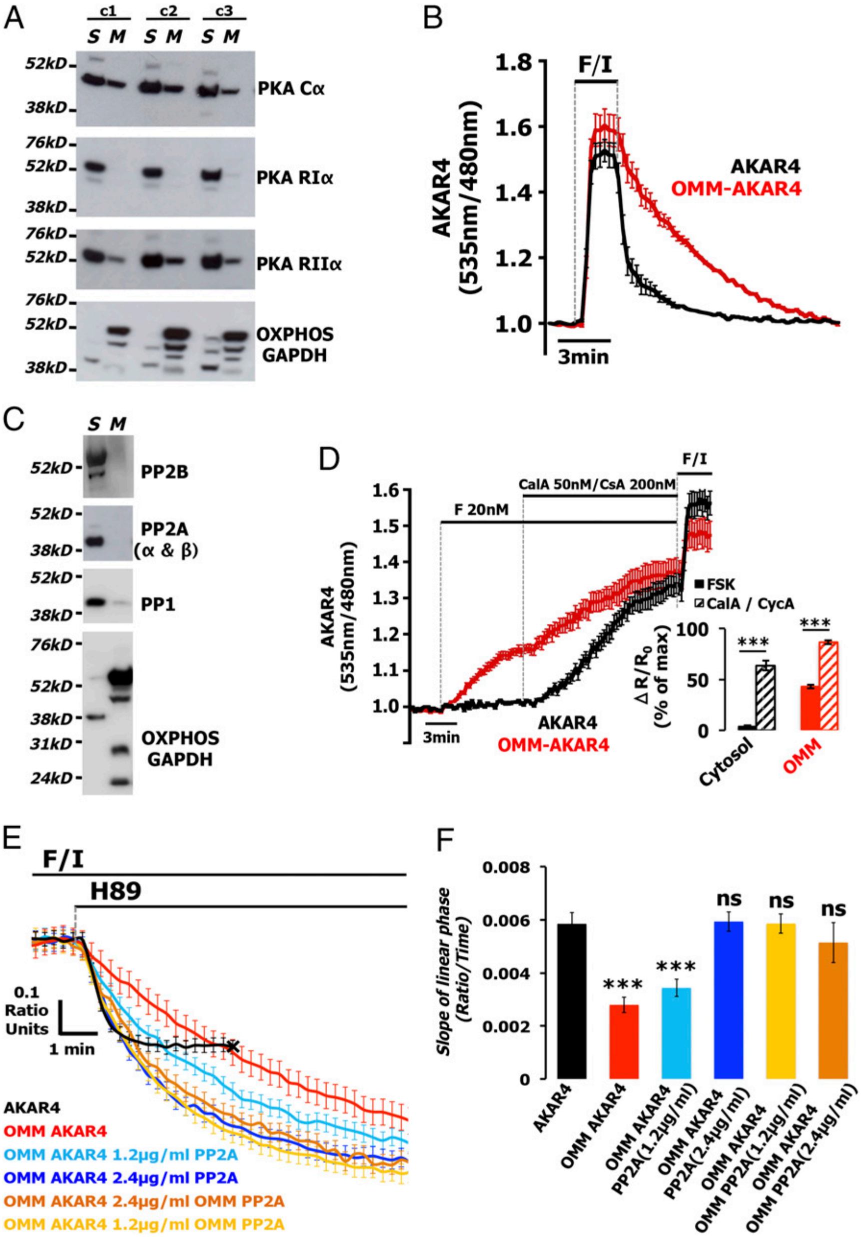

Fig. 3. Phosphatases are responsible for the different AKAR4 responses between the cytosol and OMM in NRVMs. (*A*) Western blotting of PKA components in soluble (S) and mitochondrial (M) fractions from three independent primary NRVM cultures. An antibody mixture against the rodent OXPHOS subunits and GAPDH assessed purity of mitochondria and cytosol, respectively. (*B*) PKA-dependent phosphorylation kinetics measured by OMM-AKAR4 (red trace) or cytosolic AKAR4 (black trace) in NRVMs. Challenge with 20 μM Fsk and 100 μM IBMX (F/I) resulted in saturation of both sensors. Upon rinsing the stimuli, the termination kinetics of the two sensors (depending on phosphatases) was drastically different, with OMM-AKAR4 being the slower of the two. Shown is an experiment representative of at least three independent repeats. (*C*) Western blotting testing the presence of PP2B, PP2A, and PP1 in soluble and mitochondrial fractions from primary NRVM cultures. An antibody mixture against the rodent OXPHOS subunits and GAPDH assessed the purity of mitochondria and cytosol, respectively. Shown is an experiment representative of three independent experiments. (*D*) Coculture of NRVMs expressing AKAR4 or OMM-AKAR4 challenged with Fsk (20 nM) followed by CalA (50 nM) and CsA (200 nM) to block phosphatases. Data shown are the average ± SEM of 39 AKAR4-expressing cells and 21 OMM-AKAR4-expressing cells in six independent experiments. ***$P < 0.001$). (*E*) HeLa cells expressing AKAR4 or OMM-AKAR4 or coexpressing OMM-AKAR4 with PP2Aα 1.2 μg/mL or 2.4 μg/mL (light and dark blue traces, respectively) or OMM-PP2Aα 1.2 μg/mL or 2.4 μg/mL (yellow and orange traces, respectively) were treated with Fsk 20 μM combined with IBMX 100 μM (F/I) to saturate the sensors. The addition of H89 inhibited PKA, unveiling the phosphatase effect on OMM-AKAR4. Overexpression of PP2Aα 1.2 μg/mL (22 cells) only marginally affected the dephosphorylation rate of OMM-AKAR4, whereas PP2Aα 2.4 μg/mL (22 cells), OMM-PP2Aα 1.2 μg/mL (56 cells), and 2.4 μg/mL (16 cells) significantly accelerated dephosphorylation, bringing it near that of AKAR4. Data shown are the average ± SEM of 32 AKAR4-expressing and 68 OMM-AKAR4–expressing cells. (*F*) Statistical analysis of the OMM-AKAR4 dephosphorylation rate based on the initial slope (approximately the first 90 s) of the ratio decrease after inhibiting PKA using 30 μM H89. Data are expressed as mean ± SEM; cell numbers are as in *E*. ***$P < 0.001$; ns, not significant.

CalA alone was sufficient to raise AKAR4 phosphorylation in both compartments to the same level attained with the pharmacological blockade of all three phosphatases using CalA and CsA (Fig. 3*D*). Selective inhibition of PP2B by 200 nM CsA alone did not affect the responses of AKAR4 or OMM-AKAR4 (*SI Appendix*, Fig. S4*D*), while in control experiments 200 nM CsA produced detectable (albeit mild) changes in the phosphorylation patterns detected by Western blotting experiments (*SI Appendix*, Fig. S4*E*), indicating that PP2B is active and is effectively blocked by 200 nM CsA. These results taken together suggest that in NRVMs PP2B plays only a marginal role in shaping PKA phosphorylation of OMM-targeted proteins/sensors.

Our real-time imaging experiments (Fig. 3*B*) demonstrate that PKA-dependent phosphorylation of AKAR4-based sensors in the cytosol and at the OMM reverse with different kinetics. Given that NRVM mitochondria have negligible levels of phosphatases (Fig. 3*C*), we hypothesized that dephosphorylation of OMM-tethered PKA targets is controlled mainly by their stochastic interaction with the phosphatases of bulk cytosol, following diffusion-limited, second-order reaction kinetics. We reasoned that if this were the case, increasing phosphatase levels in the cytosol or, alternatively, targeting phosphatases to the OMM should accelerate OMM-AKAR4 dephosphorylation. To test this, we generated an OMM-targeted human phosphatase 2 catalytic subunit isozyme alpha (PP2Aα) and exogenously expressed untagged PP2Aα or its OMM-targeted version (OMM-PP2Aα) together with OMM-AKAR4. We compared the rate of OMM-AKAR4 dephosphorylation with that of OMM-AKAR4 or AKAR4 in cells without additional phosphatase activity (empty vector). These experiments were performed using two levels of PP2Aα and OMM-PP2Aα: low (by transfecting 1.2 µg of plasmid DNA/mL) and high (2.4 µg of plasmid DNA/mL). As shown in Fig. 3*E*, overexpression of PP2Aα at the lower concentration (light-colored traces) had only a minor effect on the rate of dephosphorylation of OMM-AKAR4. In contrast, high levels of PP2Aα (dark-colored traces) produced markedly faster OMM-AKAR4 dephosphorylation that approached that of soluble AKAR4. Interestingly, overexpression of OMM-PP2Aα at either low or high level accelerated the rate of OMM-AKAR4 dephosphorylation. To better compare the effect of the various constructs on OMM-AKAR4 dephosphorylation rates, we calculated the initial slope of the ratio decrease during the first 90-s interval upon PKA inhibition. This analysis (Fig. 3*F*) shows that OMM-AKAR4 can be dephosphorylated as rapidly as AKAR4 in cells overexpressing high levels of PP2Aα or either low or high levels of OMM-PP2Aα.

During our single-cell and in vitro experiments, we detected higher starting ratios for OMM-AKAR4 than for AKAR4 (2.75 ± 0.05 and 1.72 ± 0.036, respectively) (*SI Appendix*, Fig. S2), which may suggest higher basal PKA activity at the OMM. This observation is in line with the observation that upon PKA inhibition OMM-AKAR4 reached ratio levels that were lower than those of AKAR4 (Fig. 3*E*). To test this possibility further, we measured the starting ratio of cells expressing AKAR4 or OMM-AKAR4 alone as well as in cells overexpressing exogenous phosphatases. Overexpression of the various PP2Aα constructs had a significant effect on the starting ratio of OMM-AKAR4 (*SI Appendix*, Fig. S5), demonstrating that the higher starting levels of this sensor depend at least in part on higher basal PKA-dependent phosphorylation at the OMM.

We then investigated the biological significance of the higher basal PKA activity at the OMM. Given the well-documented effects of PKA on the balance between mitochondrial fission and fusion (29, 32), we investigated mitochondrial morphology. For these experiments, we used constructs at the concentrations that similarly affected the OMM-AKAR4 starting ratio, 2.4 µg/mL for PP2Aα and 1.2 µg/mL for OMM-PP2Aα. As shown in *SI Appendix*, Fig. S6*A*, the two constructs did not alter the levels of endogenous PP2A and produced the expected expression levels and molecular weight in Western blot experiments performed using a PP2A-specific antibody. We also performed immunofluorescence experiments to confirm the localization of OMM-PP2Aα at the OMM. During these experiments we noticed that OMM-PP2Aα expression generated a fragmented mitochondrial phenotype *SI Appendix*, Fig. S6*B*. To further test the result that changes in basal phosphorylation at the OMM affect mitochondrial morphology, we transfected HeLa cells with PP2Aα or OMM-PP2Aα together with a mitochondrial marker (mito-YFP), and assessed mitochondrial morphology using confocal microscopy 18–24 h after transfection. As shown in *SI Appendix*, Fig. S6*C* and quantified in *SI Appendix*, Fig. S6*C*, *Inset*, either construct induced mitochondrial fragmentation.

Phosphatases Contribute to the Functional Specificity of the cAMP/PKA Axis in Cardiac Myocytes. The data shown in Fig. 3 support the hypothesis that high levels of phosphatases in the soluble fractions of the cell minimize the degree of nonspecific phosphorylation of PKA targets during stimuli that are targeted for evoking significant PKA-dependent phosphorylation in specific subcellular compartments such as the OMM. To test this hypothesis, we investigated the functional effects of our experimental stimuli (low levels of Iso and Fsk) on NRVMs using mitochondrial length as a readout of PKA actions at the OMM (33) and cAMP response element-binding protein (CREB)-dependent transcription as a readout of the soluble PKA targets (34).

We tested whether phosphorylation increases specifically at the OMM PKA domain result in mitochondrial elongation. For these experiments, NRVMs were treated with low levels of Iso (100 pM) or Fsk (20 nM) or were subjected to H89 (negative control) or vehicle control (DMSO). Twenty-four hours after treatment, mitochondria were labeled with MitoTracker-Red, and images were collected using fluorescence microscopy. As shown in Fig. 4*A* and quantified in Fig. 4*B*, mitochondria of NRVMs treated with low doses of cAMP-generating agonists became more elongated, while they fragmented upon PKA inhibition with H89.

It is now accepted that an increase in PKA activity results in elongated mitochondria by phosphorylating dynamin-related protein 1 (Drp1), a key regulator of mitochondrial fission (29, 33, 35). We therefore tested whether Drp1 phosphorylation at rat Drp1-S^{656} (human Drp1-S^{637}) (32) is increased in response to our stimuli. As shown in Fig. 4*C*, and in line with our functional observations, treatment with low Iso concentrations produced a small but significant increase in Drp-S^{656} phosphorylation. These data suggest that the observed mitochondrial phenotypes are Drp1 dependent, at least to some extent.

A cardinal function of PKA is the activation of the transcription factor CREB, a process that occurs in the nucleus. While cAMP can freely diffuse through nuclear pores (36), the presence of PKA holoenzymes in the nucleus is still debated (37, 38). The leading view is that PKA catalytic subunits migrate to the nucleus upon cAMP elevations (39). We hypothesized that soluble phosphatases suppress PKA-dependent protein phosphorylation in a bid to prevent off-target activation of CREB by cAMP signals that are intended for localized PKA pools (6). The soluble AKAR4 sensor equilibrates between the cytosol and nucleus (Fig. 2*D*, *Inset* and *SI Appendix*, Fig. S1*B*) and provides a unique opportunity to monitor PKA-dependent phosphorylation simultaneously in the same cell. As shown in Fig. 4*D* and Movie S2, in dose–response experiments using Fsk, PKA-dependent phosphorylation of AKAR4 was comparable in the two compartments, indicating that phosphatase activity in the nucleus mirrors that in the cytosol. As expected, low doses of Fsk (20 nM) did not induce any measurable phosphorylation of AKAR4 in the cytosol or the nucleus; however, upon phosphatase inhibition, the nuclear fraction of AKAR4 responded somewhat faster than the cytosol Fig. 4*E* and Movie S3.

In line with these observations, when we treated NRVMs with low doses of Fsk (20 nM) or Iso (100 pM), we were unable to observe CREB phosphorylation at S133 [the target of PKA (40)] (*SI Appendix*, Fig. S7*A*). However, when phosphatases were inhibited by CalA (5 nM), the levels of CREB phosphorylation at S^{133} increased (*SI Appendix*, Fig. S7*B*), even with the low

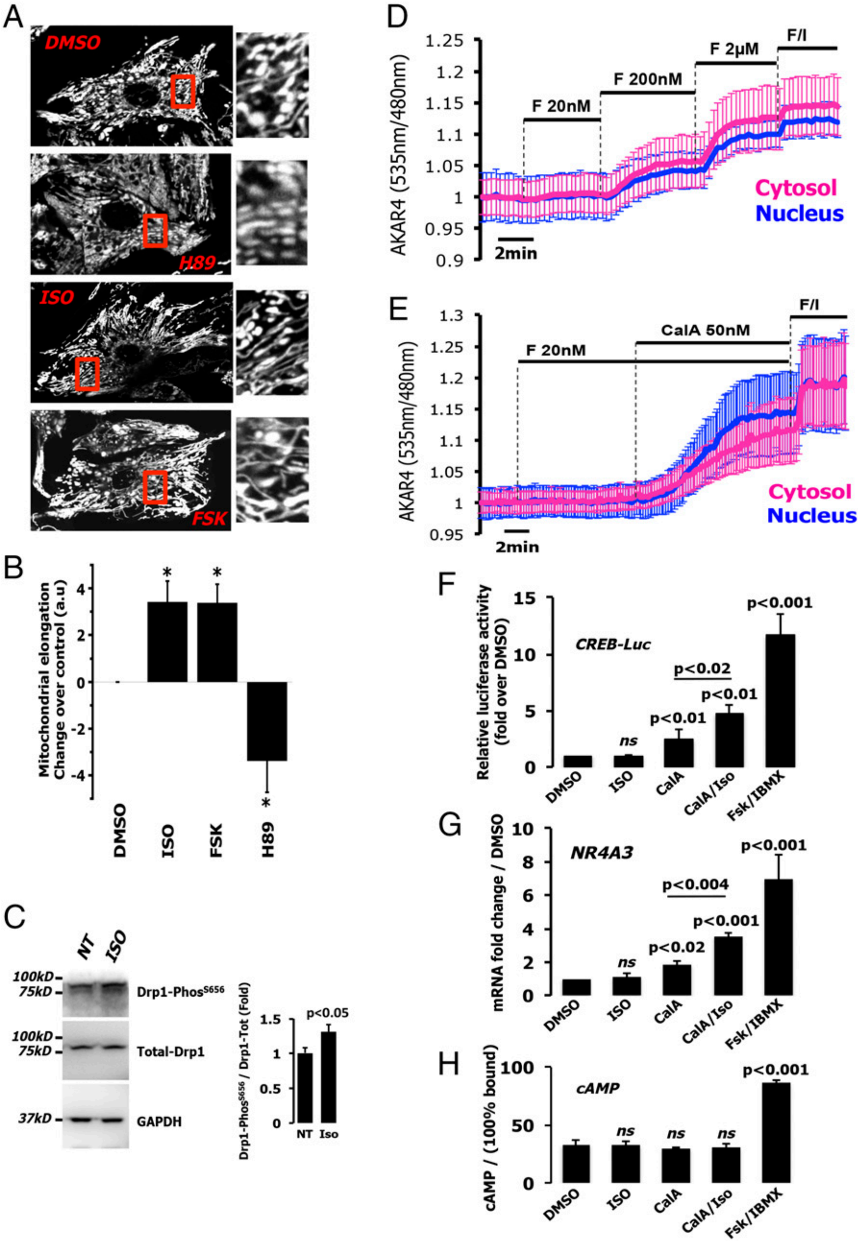

Fig. 4. Phosphatases limit PKA-dependent CREB activation in response to GPCR signals. (*A*) Confocal photomicrographs (Magnification: 60×.) of NRVMs treated for 24 h with Iso (100 pM), Fsk (20 nM), or, as control, with the PKA inhibitor H89 (10 μM) and loaded with MitoTracker-Red. (*B*) Quantification of mitochondrial elongation in NRVMs. Bar graphs show the average ± SEM of four independent blinded experiments (DMSO, 85 cells; Iso 100 pM, 49 cells; Fsk 20 nM, 53 cells; H89 10 μM, 85 cells). *$P < 0.03$). (*C*) Western blot showing Drp1 phosphorylation at S^{656} in total cell lysates of NRVMs treated with 100 pM of Iso or left untreated (NT). Total Drp1 and GAPDH were used as loading controls. (*Inset*) Intensities of phospho-Drp1 bands normalized to total Drp1 (three independent NRVM cultures). (*D*) AKAR4 responses in the nuclear (blue trace) and cytosolic (light purple trace) fractions of cells in response to increasing Fsk concentrations. Shown are representative traces of one experiment (four cells) of three independent experiments (12 cells). (*E*) AKAR4 responses in the nuclear (blue trace) and cytosolic (light purple trace) fractions of cells in response to the addition of CalA and low Fsk (20 nM). Shown are representative traces of one experiment (six cells) of six independent experiments (30 cells). (*F*) Relative quantification of CREB activity using a CREB-Luciferase reporter in NRVMs. Cells were challenged for 18–24 h with Iso (100 pM), CalA (5 nM), or a combination of both. Differences are expressed relative to the vehicle control (DMSO). All results were normalized for total protein. Bar graphs show the average ± SEM of three to five independent experiments. (*G*) Real-time PCR analysis of NR4A3 expression in NRVMs. Shown are the levels of the CREB target NR4A3 in response to different stimuli; data shown are the average ± SEM of three to five independent experiments. (*H*) Competitive ELISA immunoassay for total cAMP levels. Bar graphs show the average ± SEM of four to six independent experiments.

stimulus levels. In addition, we directly investigated the transcriptional activation of CREB by two different means: using a luciferase assay and measuring, by real-time PCR, the expression of a well-known CREB target. As shown in Fig. 4*F*, treatment with Iso (100 pM) did not induce any increase of CREB transcriptional activity measured using a luciferase-based reporter (Vector Biolabs), while a significant increase in CREB activity was measured when NRVMs were treated with Iso and CalA. These findings were confirmed by real-time PCR following the expression of the CREB target NR4A3 (nuclear receptor subfamily, group A, member 3) (41, 42). Low Iso treatment alone did not affect the expression of NR4A3, but treatment with CalA and Iso was sufficient to raise NR4A3 expression significantly (Fig. 4*G*). As shown in Fig. 4*H*, treatment with CalA did not alter the levels of total cAMP. Finally, we confirmed that receptor-independent cAMP elevations attained with low doses of Fsk (20 nM) induced CREB activation only in the presence of CalA (*SI Appendix*, Fig. S7 *C*–*E*).

Discussion

The selective phosphorylation of distinct protein targets is the defining outcome of compartmentalized cAMP/PKA signaling, but the means by which stimulus-evoked cAMP signals are able to activate selected PKA subset targets remain unclear. The canonical explanation for this observation has been that during [cAMP] elevations, off-target PKA pools remain deactivated by the enzymatic activity of PDEs, which maintain low ambient [cAMP] levels outside the target compartment (43, 44). While convincing experimental evidence proves that PDEs are important for curtailing the spatial distribution of cAMP, it is debatable whether PDE activity alone is sufficient to generate sharp cAMP signaling microdomains such as those inferred from downstream functional readouts. Arguing against microdomains being solely dependent on PDEs are computational models which consistently show that, even at restricted cAMP diffusivities (between 10 and 35 $\mu m^2 \cdot s^{-1}$) (45, 46), the distribution of mobile messenger, and hence its remit of targets, cannot be sufficiently restricted by PDE activity without implicating additional factors in the cAMP/PKA axis (13, 47). Here we provide evidence, using FRET-based measurements (Fig. 2 *A*–*D*) and biochemistry (Fig. 2*E* and *SI Appendix*, Fig. S3*D*) in HeLa cells and NRVMs, that [cAMP] elevations are able to activate OMM-tethered PKA targets robustly without engaging PKA substrates en route, and we present a kinetic explanation for this apparent paradox.

By comparing [cAMP]- and PKA-dependent phosphorylation-imaging results (Fig. 2), we demonstrate that the differential activation of PKA targets in the cytosol and at the OMM depends on the kinetics of dephosphorylation by phosphatase enzymes (Fig. 3), the final terminators of the cAMP/PKA signaling cascade. Thus, PKA targets that more readily undergo dephosphorylation will be less strongly (or not at all) activated in response to similar [cAMP] elevations. A simplified equation describing the dynamics of phosphorylated protein fractions (F_{PP}) is

$$\frac{dF_{PP}}{dt} = k_{on} \times [cAMP] \times (1 - F_{PP}) - k_{off} \times F_{PP} \qquad [1]$$

We define k_{on} as the rate constant describing the ensemble of processes that lead to phosphorylation at a given cAMP level, while k_{off} is the rate constant describing the phosphatase-catalyzed dephosphorylation process.

At steady state ($dF_{PP}/dt = 0$), we obtain

$$F_{PP} = \frac{[cAMP]}{[cAMP] + K} \qquad [2]$$

where K is defined as k_{off}/k_{on}. By replotting the data from Fig. 2 *A*–*D* (responses to Fsk and Iso) to obtain the relationship between [cAMP] variations and PKA-dependent phosphorylation (*SI Appendix*, Fig. S8), we found that K is approximately fourfold lower at the OMM than at the cytosol. We then used the experimental data of Fig. 3*D* to calculate the rate of target phosphorylation (which would be related to k_{on}) at the OMM and soluble fractions upon phosphatase inhibition and found that they were not statistically different between the two compartments: 0.676×10^{-3}/s (SEM: 0.05×10^{-3}) for OMM-AKAR4 and 0.701×10^{-3}/s (SEM: 0.047×10^{-3}) for AKAR4. On the other hand, the rate constant k_{off} can be estimated from the dephosphorylation process triggered by PKA inhibition, shown in Fig. 3*E*. The dephosphorylation reaction at the OMM (time constant 351.9 ± 44.5 s) was one order of magnitude slower than in the cytosol (time constant 25.5 ± 2.2 s), which is consistent with the observed differences in the magnitude of K. Since we found no evidence for OMM-tethered Ser/Thr phosphatases, we postulate that the dephosphorylation of both cytosolic and OMM-bound phosphoproteins relies on pools of soluble phosphatases, mainly PP1 and PP2A. A plausible explanation for the greater persistence of phosphorylation at the OMM relates to the immobilized state of OMM-tethered PKA targets. It is well established that immobilized enzymes produce slower reactions than their soluble counterparts, a kinetic disadvantage which can be described by an effectiveness factor (48), and a similar framework will apply to immobilized substrates.

For diffusion-limited reactions (the likely form of interaction involving two macromolecules, phosphatase and phosphoprotein), immobilizing PKA targets at the OMM will reduce their rate constant of dephosphorylation for at least three reasons. First, dephosphorylation at the OMM (e.g., OMM-AKAR4) requires the soluble phosphatase to diffuse toward its immobilized substrate, which is inherently slower than a system involving a diffusible enzyme and diffusible substrate (e.g., soluble AKAR4). This factor can account for a twofold decrease in k_{off} at the OMM since effective diffusivity of an enzyme–substrate system involving two macromolecules is halved when one of the components becomes fixed. Second, an immobilized substrate has limited rotational freedom, which restricts the incidence of viable interactions with the enzyme's active site. In contrast, cytosolic phosphoproteins demonstrate rotational diffusion, which facilitates interactions with soluble phosphatases. Third, it is plausible that phosphatases are less accessible to the OMM due to steric or physicochemical hindrance. In summary, OMM-tethered PKA targets are less susceptible to dephosphorylation because of the kinetics underpinning their interaction with common pool phosphatases. A similar phenomenon is likely to apply also to other PKA targets tethered to other membranes, particularly those with a high density of proteins.

We propose that compartments of differing susceptibility to dephosphorylation may attain distinct levels of PKA-dependent phosphorylation, even at the same level of [cAMP], highlighting the critical importance of phosphatases to signal compartmentalization.

From a functional point, we demonstrate that, due to the limited phosphatase access, the OMM harbors higher PKA-dependent phosphorylation (as measured by OMM AKAR4), which is observed even at basal conditions and that perturbing this equilibrium in favor of dephosphorylation leads to severe mitochondrial fractionation (*SI Appendix*, Fig. S6 *B* and *C*). We further show that the role of soluble phosphatases is equally important during the application of cAMP-producing agonists. In response to low cAMP elevations, PKA-dependent phosphorylation of target proteins is dampened at both the cytosol and the nucleus. Importantly, we find that phosphatase activity in the latter mirrors that of the cytosol and curtails PKA-dependent activation of CREB (Fig. 4 *F*–*H* and *SI Appendix*, Fig. S7 *C*–*E*), while the same cAMP-generating stimuli have a profound effect on mitochondrial morphology (Fig. 4 *A* and *B*) (49).

By identifying phosphatases as central contributors to the compartmentalization of PKA actions, we add another regulatory layer that is downstream of, and may occur in parallel with, the PDE-dependent compartmentalization of the messenger itself, as parts of the mechanisms that define functionally distinct cAMP signaling microdomains.

It is noteworthy that the phosphatase–phosphoprotein interaction is not a canonical substrate–enzyme reaction like that between cAMP and PDEs, because the substrate is predicted to diffuse no faster than the enzyme. The phosphatase–phosphoprotein system is therefore more likely to underpin the sharply demarcated differences in target activation compared with that attainable with the considerably more mobile cAMP.

While the role of phosphatases in shaping localized cAMP signals has been underappreciated, mathematical models and experimental data (50, 51) convincingly demonstrate the role of phosphatases in signal transduction. Indeed, our data are in line with models made by Heinrich et al. (50), who have suggested that kinases/phosphatases equilibrium may play a supplementary role in regulating overall signal dynamics. While the actions of phosphatases may appear expensive in energetic terms for the cell, a recent estimate suggests that the phosphorylation–dephosphorylation cycle of proteins consumes a very small fraction of cellular ATP (<0.01%) (51, 52). The apparently futile cycle of phosphorylation–dephosphorylation of off-target proteins during transient cAMP increases would be a price worth paying for compartmentalized cAMP/PKA signaling.

Materials and Methods

Reagents. Fsk, IBMX, CalA, CsA, and H89 were purchased from Tocris Bioscience. High-glucose DMEM, MEM199, horse serum, newborn calf serum, penicillin/streptomycin, glutamine, MitoTracker-Red, and primers/probes and reagents for real-time PCR were purchased from Invitrogen. Collagenase A was from Roche; laminin (mouse) was from BD Biosciences. Unless otherwise specified, all other reagents were purchased from Sigma.

Primary Cardiac Myocyte Isolation Transfection/Infection and Coculture. NRVMs were isolated from 1- to 3-d-old Sprague–Dawley pups as previously described (44, 53). Briefly, animals were killed following the schedule 1 procedure in line with the protocols approved by the University of Oxford. The hearts were rinsed and digested using a mix of collagenase (0.45 mg/mL) and pancreatin (1.25 mg/mL). After digestion the isolated cells were resuspended in medium 1 (M1) (DMEM 67%; M-199 17.9%; horse serum 10%; newborn calf serum 5%; glutamine 200 mM; penicillin/streptomycin 0.1%). To remove the majority of fibroblasts and select the NRVMs, cells were allowed to settle for 2 h in uncoated 6-cm tissue-culture Petri dishes in the incubator at 37 °C; the fibroblasts attached to the dishes, and the cardiac myocytes did not. During this step each 6-cm dish was infected with adenoviral particles bearing one of our FRET sensors (cyto-AKAR4, cyto-H187, OMM-AKAR4, or OMM-H187). Two hours after infection cardiac myocytes were carefully collected and washed four times with excess ADS buffer (Hepes 20 mM; NaH_2PO_4 0.8 mM; KCl 5.3 mM; $MgSO_4$ 0.4 mM; glucose 5 mM). After the washings cells were resuspended in M1, and the individually infected populations were mixed in pairs and plated onto laminin (20 μL/mL)-coated glass coverslips. Eighteen hours after isolation cells were washed with ADS buffer, and the medium M1 was replaced with medium 2 (M2) (DMEM 75%; M-199 17%; horse serum 5%; newborn calf serum 0.5%; glutamine 200 mM; penicillin/streptomycin 1%).

HeLa cells were plated onto 6-cm Petri dishes, and 24 h after seeding cells (typically 500–1,000 ng of plasmids expressing the different sensors) were transfected using Lipofectamine 2000 according to the provider's protocol. Six hours after transfection cells were released using trypsin, and the populations transfected with different sensors were mixed and plated onto sterile glass coverslips. Cells were imaged 24–48 h later as described above.

FRET Imaging. NRVMs were cultured onto glass coverslips coated with laminin; 18–24 h after plating cells were mounted onto an open perfusion chamber RC-25F (Warner Instruments). Cells were perfused using a homemade gravity-fed perfusion system with a velocity of 1 mL/min. Cells were bathed in Ringer's modified buffer: NaCl 125 mM; KCL 5 mM; Na3PO4 1 mM; $MgSO_4$ 1 mM; Hepes 20 mM; glucose 5.5 mM; CaCl2 1 mM; pH adjusted to 7.4 using 1 M NaOH. Experiments were performed on an Olympus IX71 inverted microscope equipped with a beam-splitter (OptoSplit II) and a CCD camera (CoolSNAP HQ2). An LED source excited the cyan fluorescent proteins (cerulean for AKAR4 or mTurquoise for H187) at 430 nm; the emission fluorescence was collected for both donor and acceptor fluorophores at 480 nm and 545 nm, respectively, every 8–15 s. Automatic image collection and preliminary analysis were performed using MetaFluor software (Molecular Devices). Raw data were transferred to Excel (Microsoft) for background subtraction and generation of the ratios; graphs were generated by Origin software (OriginLab).

Mitochondrial Isolation, Proteinase K Treatment, and Western Blotting. Mitochondrial and soluble fractions from populations of NRVMs were isolated using the Qproteome Mitochondria Isolation Kit (37612; Qiagen). Proteinase K digestion was performed in solution as directed by the manufacturer (Sigma). For Western blotting we used precast gels (Bolt Invitrogen) to dissolve 10–40 μg of total cell lysate. Briefly, NRVMs were cultured for 2–3 d at 5×10^6 cells per 10-cm culture Petri dish. If cells required treatment with pharmacological agents, this was performed immediately before the mitochondrial isolation process. The Qproteome Mitochondria Isolation Kit (37612; Qiagen) was used to isolate mitochondria according to the manufacturer's recommended protocol with the sole modification that all required buffers were complemented with phosphatase inhibitors (Roche). The two protein fractions we compare throughout the paper (soluble/cytosolic and mitochondria) were obtained in two different stages of the Qproteome kit. Soluble/cytosolic fractions were obtained after bland lysis of the cells (step 1 of protocol) and low-speed centrifugation. During this lysis passage the plasma membrane is compromised enough to release the soluble/cytosolic proteins that are unbound while retaining all structures and organelles. We refer to this fraction as the "soluble/cytosolic fraction" and compare it with the mitochondria-enriched fraction obtained at the final step of the Qproteome protocol. To identify the mitochondrial compartment where phosphorylation was more prominent following our treatments, we used low concentrations of Proteinase K (10–30 μg/mL) to degrade OMM proteins exposed to the cytosol. Treatments were performed on ice for 20 min; then the activity of the enzyme was quenched using PMSF (1 mM). The final products of the mitochondrial isolation and the complementary soluble/cytosolic components were quantified to determine accurately the protein concentration of each. Bradford reagent (B6916-500ML; Sigma) was used along with a PerkinElmer LAMBDA Bio+ spectrophotometer. Equal quantities of protein for each treatment were dissolved in acrylamide gels (Invitrogen), and after transfer, the PVDF membranes were probed for PKA phosphorylated substrates using a specific antibody recognizing primarily the PKA phosphorylated consensus $RRx(T/Y)^P$ (9624; Cell Signaling Tec.). Specific antibodies against PKA-Cα (sc-903; Santa Cruz), PKA RIα (610609; BD Biosciences), PKA RIIα (sc-908; Santa Cruz), PP2A (α and β) (ab32141; Abcam), PP1 (sc-7482; Santa Cruz), S133-phospho CREB (sc-7978; Santa Cruz), CREB (48H2; Cell Signaling Technology), GFP (sc-9996-HRP; Santa Cruz), Drp1 phospho-S637 (4867; Cell Signaling Technology), total Drp1 (ab56788; Abcam), Phospho-(Ser/Thr) (no. 9631; Cell Signaling Technology), and c-Myc (9E10; Thermo Scientific) were also used. As control for mitochondrial enrichment and the effectiveness of Proteinase K treatment, we used a Tom20 antibody (sc-11415; Santa Cruz) and a mixture of monoclonal antibodies recognizing several OXPHOS components (ab1104413 for NRVMs and ab110411 for HeLa; Abcam). An antibody against GAPDH (sc-166574; Santa Cruz) was used as cytosolic marker. The GADPH and OXPHOS antibodies were used separately or were mixed for some of the experiments. HRP-conjugated secondary antibodies against rabbit (W401B) or mouse (W402B) were purchased from Promega. Dilutions used for all primary antibodies were 1:1,000–1:3,000; dilutions for the secondary antibodies were 1:3,000–1:8,000.

Evaluation of Mitochondrial Fusion. Quantitative evaluation of mitochondrial fusion was performed by computing a mitochondria distribution parameter R as in (54), combined with a spatial smoothing filtering procedure. For each cell, R was computed as follows: MitoTracker or mito-YFP fluorescence, F, averaged within a pixel region of interest (ROI) covering the whole cell area, was divided by the highest pixel value in the ROI, Fmax, to obtain R = F/Fmax. R has values between 0 and 1 and was expected to reach higher values in a cell with homogeneous mitochondrial distribution, as F is closer to Fmax in such cells than in cells displaying mitochondrial clustering due to fusion. This difference can be significantly amplified by applying, a Gaussian smoothing filter on the MitoTracker fluorescence image before computing R. For each sample we analyzed a minimum of 56–89 cells from four independent primary myocyte cultures. The process was blinded in all steps, i.e., treatment, acquisition, and analysis.

Luciferase Assay. To follow CREB activity we used a commercially available CREB reporter adenoviral system Ad-CREB-Luc (Vector Biolabs). The infection efficiency of adenoviral constructs in NRVMs was calculated to be near 90–95% after 48 h (53). Freshly isolated NRVMs were counted and resuspended in medium at a concentration of 300×10^5/mL. To ensure equal infection, the cells in suspension were complemented with the appropriate amount of Ad-CREB-Luc, and after mixing an equal volume of the mixture (1 mL) was seeded in 12-well plates coated with laminin. Twenty-four hours after plating cells were treated with Iso (100 pM), CalA (5 nM), Fsk (20 nM), or combinations thereof. DMSO was used as vehicle control, and Fsk (20 μM) combined with IBMX (100 μM) served as a positive control. Twenty-four hours after treatment cells were lysed, and luciferase expression was determined using the Dual-Luciferase Reporter Assay System (Promega). Luciferase signals were normalized to total protein content.

Statistical Analyses. Values are expressed as the mean ± SEM, and error bars in figures represent the SEM. Values were calculated from at least triplicate repeats. When possible, experiments were randomized and blinded. Statistical significance was determined using unpaired Student's *t* tests. Data shown for microscopy images and Western blots are representative of three to six independent experiments.

Experimental procedures for cloning and adenovirus generation, immunofluorescence, in vitro validation of the FRET-based sensors, confocal imaging, real-time PCR, and luciferase and cAMP assays are described in *SI Appendix, Methods*.

ACKNOWLEDGMENTS. We thank Prof. Kees Jalink for the EpacH187 sensor; Prof. Roger Y. Tsien for mCherry; Prof. Jin Zhang for AKAR4; Prof. György Hajnóczky for yTOM-mCherry; Prof. Ajay Singh for PPP2CAα; Prof. Manuela Zaccolo for sharing instrumentation and helpful discussions; Dr. Valentina Prando and Dr. Salvatore Antonucci for providing NRVMs for control experiments; Dr. Alzbeta Hulikova for assistance with confocal microscopy and for reading the manuscript; and Dr. Kerrie Ford for proofreading the manuscript. Work done by E.P. was supported by Canadian Institutes of Health Research Operating Grant 201603PJT-365052 (to L.P.). Work done in the T.P. laboratory is supported by Telethon Foundation Grant GGP16029, Consiglio Nazionale delle Ricerche Project Invecchiamento, European Strategy Forum on Research Infrastructures Project Roadmap, and Italian Ministry of University and Education Grant 2015W2N883. K.L. was the recipient of British Heart Foundation Centre of Research Excellence, Oxford Fellowship RE/13/1/30181.

1. Lefkimmiatis K, Zaccolo M (2014) cAMP signaling in subcellular compartments. *Pharmacol Ther* 143:295–304.
2. Kritzer MD, Li J, Dodge-Kafka K, Kapiloff MS (2012) AKAPs: The architectural underpinnings of local cAMP signaling. *J Mol Cell Cardiol* 52:351–358.
3. Scott JD, Dessauer CW, Taskén K (2013) Creating order from chaos: Cellular regulation by kinase anchoring. *Annu Rev Pharmacol Toxicol* 53:187–210.
4. Lomas O, Zaccolo M (2014) Phosphodiesterases maintain signaling fidelity via compartmentalization of cyclic nucleotides. *Physiology (Bethesda)* 29:141–149.
5. Di Benedetto G, et al. (2008) Protein kinase A type I and type II define distinct intracellular signaling compartments. *Circ Res* 103:836–844.
6. Haj Slimane Z, et al. (2014) Control of cytoplasmic and nuclear protein kinase A by phosphodiesterases and phosphatases in cardiac myocytes. *Cardiovasc Res* 102: 97–106.
7. Heijman J, Dewenter M, El-Armouche A, Dobrev D (2013) Function and regulation of serine/threonine phosphatases in the healthy and diseased heart. *J Mol Cell Cardiol* 64:90–98.
8. Hinke SA, et al. (2012) Anchored phosphatases modulate glucose homeostasis. *EMBO J* 31:3991–4004.
9. Taylor SS, Buechler JA, Yonemoto W (1990) cAMP-dependent protein kinase: Framework for a diverse family of regulatory enzymes. *Annu Rev Biochem* 59: 971–1005.
10. Dostmann WR, et al. (1990) Probing the cyclic nucleotide binding sites of cAMP-dependent protein kinases I and II with analogs of adenosine 3′,5′-cyclic phosphorothioates. *J Biol Chem* 265:10484–10491.
11. Taylor SS, Ilouz R, Zhang P, Kornev AP (2012) Assembly of allosteric macromolecular switches: Lessons from PKA. *Nat Rev Mol Cell Biol* 13:646–658.
12. Hanoune J, Defer N (2001) Regulation and role of adenylyl cyclase isoforms. *Annu Rev Pharmacol Toxicol* 41:145–174.
13. Saucerman JJ, Greenwald EC, Polanowska-Grabowska R (2014) Mechanisms of cyclic AMP compartmentation revealed by computational models. *J Gen Physiol* 143:39–48.
14. Klarenbeek J, Goedhart J, van Batenburg A, Groenewald D, Jalink K (2015) Fourth-generation epac-based FRET sensors for cAMP feature exceptional brightness, photostability and dynamic range: Characterization of dedicated sensors for FLIM, for ratiometry and with high affinity. *PLoS One* 10:e0122513.
15. Larsen HE, Lefkimmiatis K, Paterson DJ (2016) Sympathetic neurons are a powerful driver of myocyte function in cardiovascular disease. *Sci Rep* 6:38898.
16. Larsen HE, Bardsley EN, Lefkimmiatis K, Paterson DJ (2016) Dysregulation of neuronal Ca2+ channel linked to heightened sympathetic phenotype in prohypertensive states. *J Neurosci* 36:8562–8573.
17. Lefkimmiatis K, Moyer MP, Curci S, Hofer AM (2009) "cAMP sponge": A buffer for cyclic adenosine 3′, 5′-monophosphate. *PLoS One* 4:e7649.
18. Maiellaro I, Lefkimmiatis K, Moyer MP, Curci S, Hofer AM (2012) Termination and activation of store-operated cyclic AMP production. *J Cell Mol Med* 16:2715–2725.
19. Lefkimmiatis K, Leronni D, Hofer AM (2013) The inner and outer compartments of mitochondria are sites of distinct cAMP/PKA signaling dynamics. *J Cell Biol* 202: 453–462.
20. Burdyga A, Lefkimmiatis K (2015) Simultaneous assessment of cAMP signaling events in different cellular compartments using FRET-based reporters. *Methods Mol Biol* 1294:1–12.
21. Dorsam RT, Gutkind JS (2007) G-protein-coupled receptors and cancer. *Nat Rev Cancer* 7:79–94.
22. Nikolaev VO, et al. (2010) Beta2-adrenergic receptor redistribution in heart failure changes cAMP compartmentation. *Science* 327:1653–1657.
23. Depry C, Allen MD, Zhang J (2011) Visualization of PKA activity in plasma membrane microdomains. *Mol Biosyst* 7:52–58.
24. Giansanti P, Stokes MP, Silva JC, Scholten A, Heck AJ (2013) Interrogating cAMP-dependent kinase signaling in Jurkat T cells via a protein kinase A targeted immune-precipitation phosphoproteomics approach. *Mol Cell Proteomics* 12: 3350–3359.
25. Acin-Perez R, et al. (2009) Cyclic AMP produced inside mitochondria regulates oxidative phosphorylation. *Cell Metab* 9:265–276.
26. Means CK, et al. (2011) An entirely specific type I A-kinase anchoring protein that can sequester two molecules of protein kinase A at mitochondria. *Proc Natl Acad Sci USA* 108:E1227–E1235.
27. Di Benedetto G, Scalzotto E, Mongillo M, Pozzan T (2013) Mitochondrial Ca^{2+} uptake induces cyclic AMP generation in the matrix and modulates organelle ATP levels. *Cell Metab* 17:965–975.
28. Redden JM, Dodge-Kafka KL (2011) AKAP phosphatase complexes in the heart. *J Cardiovasc Pharmacol* 58:354–362.
29. Cribbs JT, Strack S (2007) Reversible phosphorylation of Drp1 by cyclic AMP-dependent protein kinase and calcineurin regulates mitochondrial fission and cell death. *EMBO Rep* 8:939–944.
30. Cereghetti GM, et al. (2008) Dephosphorylation by calcineurin regulates translocation of Drp1 to mitochondria. *Proc Natl Acad Sci USA* 105:15803–15808.
31. Mehta S, et al. (2014) Calmodulin-controlled spatial decoding of oscillatory Ca2+ signals by calcineurin. *eLife* 3:e03765.
32. Chang CR, Blackstone C (2007) Drp1 phosphorylation and mitochondrial regulation. *EMBO Rep* 8:1088–1089, author reply 1089–1090.
33. Di Benedetto G, Gerbino A, Lefkimmiatis K (2018) Shaping mitochondrial dynamics: The role of cAMP signalling. *Biochem Biophys Res Commun* 500:65–74.
34. Ichiki T (2006) Role of cAMP response element binding protein in cardiovascular remodeling: Good, bad, or both? *Arterioscler Thromb Vasc Biol* 26:449–455.
35. Chang CR, Blackstone C (2007) Cyclic AMP-dependent protein kinase phosphorylation of Drp1 regulates its GTPase activity and mitochondrial morphology. *J Biol Chem* 282: 21583–21587.
36. Terrin A, et al. (2006) PGE(1) stimulation of HEK293 cells generates multiple contiguous domains with different [cAMP]: Role of compartmentalized phosphodiesterases. *J Cell Biol* 175:441–451.
37. Sample V, et al. (2012) Regulation of nuclear PKA revealed by spatiotemporal manipulation of cyclic AMP. *Nat Chem Biol* 8:375–382.
38. Yang JH, Polanowska-Grabowska RK, Smith JS, Shields CW, 4th, Saucerman JJ (2014) PKA catalytic subunit compartmentation regulates contractile and hypertrophic responses to β-adrenergic signaling. *J Mol Cell Cardiol* 66:83–93.
39. Harootunian AT, et al. (1993) Movement of the free catalytic subunit of cAMP-dependent protein kinase into and out of the nucleus can be explained by diffusion. *Mol Biol Cell* 4:993–1002.
40. Yamamoto KK, Gonzalez GA, Biggs WH, 3rd, Montminy MR (1988) Phosphorylation-induced binding and transcriptional efficacy of nuclear factor CREB. *Nature* 334: 494–498.
41. Altarejos JY, Montminy M (2011) CREB and the CRTC co-activators: Sensors for hormonal and metabolic signals. *Nat Rev Mol Cell Biol* 12:141–151.
42. Impey S, et al. (2004) Defining the CREB regulon: A genome-wide analysis of transcription factor regulatory regions. *Cell* 119:1041–1054.
43. Houslay MD (2010) Underpinning compartmentalised cAMP signalling through targeted cAMP breakdown. *Trends Biochem Sci* 35:91–100.
44. Zaccolo M, Pozzan T (2002) Discrete microdomains with high concentration of cAMP in stimulated rat neonatal cardiac myocytes. *Science* 295:1711–1715.
45. Agarwal SR, Clancy CE, Harvey RD (2016) Mechanisms restricting diffusion of intracellular cAMP. *Sci Rep* 6:19577.
46. Richards M, et al. (2016) Intracellular tortuosity underlies slow cAMP diffusion in adult ventricular myocytes. *Cardiovasc Res* 110:395–407.
47. Lohse C, et al. (2017) Experimental and mathematical analysis of cAMP nanodomains. *PLoS One* 12:e0174856.
48. Fink David J, Na T, Schultz Jerome S (1973) Effectiveness factor calculations for immobilized enzyme catalysts. *Biotechnol Bioeng* 15:879–888.
49. Merrill RA, et al. (2011) Mechanism of neuroprotective mitochondrial remodeling by PKA/AKAP1. *PLoS Biol* 9:e1000612.
50. Heinrich R, Neel BG, Rapoport TA (2002) Mathematical models of protein kinase signal transduction. *Mol Cell* 9:957–970.
51. Lemmon MA, Freed DM, Schlessinger J, Kiyatkin A (2016) The dark side of cell signaling: Positive roles for negative regulators. *Cell* 164:1172–1184.
52. Monast CS, Furcht CM, Lazzara MJ (2012) Computational analysis of the regulation of EGFR by protein tyrosine phosphatases. *Biophys J* 102:2012–2021.
53. Zoccarato A, et al. (2015) Cardiac hypertrophy is inhibited by a local pool of cAMP regulated by phosphodiesterase 2. *Circ Res* 117:707–719.
54. Spinazzi M, et al. (2008) A novel deletion in the GTPase domain of OPA1 causes defects in mitochondrial morphology and distribution, but not in function. *Hum Mol Genet* 17:3291–3302.